nanomaterials

MDPI

Communication

One-Step Synthesis of Cu_xO_y/TiO_2 Photocatalysts by Laser Pyrolysis for Selective Ethylene Production from Propionic Acid Degradation

Juliette Karpiel [1,2], Pierre Lonchambon [1], Frédéric Dappozze [2], Ileana Florea [3], Diana Dragoe [4], Chantal Guillard [2] and Nathalie Herlin-Boime [1,*]

[1] NIMBE, CEA, CNRS, Université Paris-Saclay, CEA Saclay, 91191 Gif-sur-Yvette, France
[2] Institut de Recherche Sur La Catalyse Et l'Environnement De Lyon (IRCELYON), Université Lyon 1, CNRS, Avenue Albert Einstein, 69626 Villeurbanne, France
[3] Laboratory of Physics of Interfaces and Thin Films (LPICM), Ecole Polytechnique, CNRS, Institut Polytechnique de Paris, 91128 Palaiseau, France
[4] CNRS, Institut de Chimie Moléculaire et des Matériaux d'Orsay (ICMMO), Université Paris-Saclay, 91405 Orsay, France
* Correspondence: nathalie.herlin@cea.fr

Abstract: In an effort to produce alkenes in an energy-saving way, this study presents for the first time a photocatalytic process that allows for the obtention of ethylene with high selectivity from propionic acid (PA) degradation. To this end, TiO_2 nanoparticles (NPs) modified with copper oxides (Cu_xO_y/TiO_2) were synthetised via laser pyrolysis. The atmosphere of synthesis (He or Ar) strongly affects the morphology of photocatalysts and therefore their selectivity towards hydrocarbons (C_2H_4, C_2H_6, C_4H_{10}) and H_2 products. Specifically, Cu_xO_y/TiO_2 elaborated under He environment presents highly dispersed copper species and favours the production of C_2H_6 and H_2. On the contrary, Cu_xO_y/TiO_2 synthetised under Ar involves copper oxides organised into distinct NPs of ~2 nm diameter and promotes C_2H_4 as the major hydrocarbon product, with selectivity, i.e., C_2H_4/CO_2 as high as 85% versus 1% obtained with pure TiO_2.

Keywords: photocatalysis; ethylene; hydrocarbons; hydrogen; titanium dioxide; propionic acid

check for updates

Citation: Karpiel, J.; Lonchambon, P.; Dappozze, F.; Florea, I.; Dragoe, D.; Guillard, C.; Herlin-Boime, N. One-Step Synthesis of Cu_xO_y/TiO_2 Photocatalysts by Laser Pyrolysis for Selective Ethylene Production from Propionic Acid Degradation. *Nanomaterials* **2023**, *13*, 792. https://doi.org/10.3390/nano13050792

Academic Editor: Andreu Cabot

Received: 26 January 2023
Revised: 10 February 2023
Accepted: 14 February 2023
Published: 21 February 2023

Copyright: © 2023 by the authors. Licensee MDPI, Basel, Switzerland. This article is an open access article distributed under the terms and conditions of the Creative Commons Attribution (CC BY) license (https://creativecommons.org/licenses/by/4.0/).

1. Introduction

Ethylene (C_2H_4) is a key molecule in the chemical industry. About 75% of petrochemical products are obtained from this light olefin, including intermediates such as ethylene glycol and polymers such as polyethylene or polyvinyl chloride [1–3]. Currently, ethylene is mostly produced from the steam cracking of fossil fuels. However, besides relying on non-sustainable feedstock and being extremely polluting, such a method is one of the most energy-consuming processes in the chemical sector as it requires considerable working temperatures (T > 750 °C) [4,5].

Hence, researchers are developing new strategies for cleaner and lower-cost ethylene production without the use of hydrocarbons. Among them, heterogeneous photocatalysis attracts great attention for being an oxidation process operating at ambient temperature and atmospheric pressure, thus offering favourable perspectives for sustainable organic synthesis using solar light [6]. Nonetheless, very few research articles describe the photocatalytic production of ethylene [7–12]. Despite its high relevance, CO_2 photocatalytic reduction to C_2H_4 is very challenging as it requires effective C-C coupling and a multi-electron reaction process [7]. Another strategy to form ethylene consists of the photocatalysis of carboxylic acids operating in an anaerobic medium. Photo-decarboxylation of such acids (acetic, propionic, butanoic, etc.) mainly produces CO_2, H_2, and alkanes [8–13] using TiO_2 or TiO_2-based nanomaterials decorated with metal co-catalysts to promote quantum yield

maximization [14]. In some cases, alkenes were also detected. Kraeutler and Bard [11] identified ethylene traces from propionic acid decarboxylation with $Pt/TiO_{2,}$ which were confirmed afterwards in the Betts et al. study using TiO_2 Evonik P25 [12]. Scandura et al. enhanced propene and ethylene selectivities from butyric acid and propionic acid photoreforming, respectively, with Au/TiO_2 compared to Pt/TiO_2 [10]. However, despite the use of onerous noble metals, alkenes were each time detected in trace amounts.

Herein, we report for the first time the selective photocatalytic production of ethylene from the valorisation of propionic acid using TiO_2 modified with copper nanoparticles under UVA light. Specifically, TiO_2 and Cu_xO_y/TiO_2 photocatalysts were elaborated using a laser pyrolysis technique, an industrial-scale process that enables a one-step and continuous synthesis of nanopowders at several grams per hour. The impact of the laser pyrolysis operating atmosphere (Ar, He) on the morphology and the material photocatalytic performances were studied. Propionic acid (PA) was selected as the model molecule; this volatile fatty acid can be obtained from the fermentation of organic wastes [15]. This work provides a new method for sustainable ethylene production with low energy consumption and low-cost photocatalysts.

2. Materials and Methods

2.1. Chemicals

Titanium (IV) isopropoxide (TTIP, ≥97% purity), ethylacetate (99.8% purity) and copper (II) acetylacetonate ($Cu(acac)_2$, ≥97% purity) were purchased from Sigma-Aldrich, Darmstadt, Germany. Pure o-xylene was supplied from Fisher, Waltham, MA, USA. Helium He, argon Ar and ethylene C_2H_4 gases were supplied by Air Products and Chemicals, Allentown, PA, USA. All the reactants were used without further purification. Propionic acid (PA) was obtained from Sigma-Aldrich, Darmstadt, Germany (≥99.5% purity).

2.2. Chemicals Synthesis of TiO_2 and Cu_xO_y/TiO_2 Nanoparticles

The synthesis of TiO_2 and Cu modified TiO_2 photocatalysts was performed with the laser pyrolysis technique under He or Ar gas. This method permits the continuous and direct production of nanopowders and is described elsewhere [16]. Briefly, its principle is based on the orthogonal interaction of an infrared CO_2 laser (10.6 µm) in continuous mode with a gaseous or liquid mixture of reagents. The laser was focused by means of a cylindrical lens, resulting in a horizontal beam of about 30 mm. For the synthesis of reference samples (TiO_2), the mixture consisted of 175 g of liquid titanium (IV) isopropoxide (TTIP) dissolved in a 150 mL o-xylene/ethylacetate solution (65 vol%/35 vol%). Dissolution of 4.13 g of $Cu(acac)_2$ (copper (II) acetylacetonate) into the previous mixture permitted us to obtain Cu_xO_y/TiO_2 particles with a theoretical Cu content equalling 2.0 wt% regarding the final nanomaterials. The resulting liquid was converted into microdroplets with a spray generator, regulating the mixture at 30 °C. The liquid droplets were transported into the reactor zone through a carrier gas (He or Ar) at 2000 $cm^3.min^{-1}$ flow. A sensitiser gas (C_2H_4, 800 $cm^3.min^{-1}$) was added to the carrier gas to enhance the laser absorption of the precursors. The reaction zone was confined by He or Ar inert gas flow. The CO_2 laser power (measured under inert gas) was set to 670 W and the pressure inside the reactor was regulated to 740 Torr. The powders were collected on filters located downstream.

The TiO_2 and Cu_xO_y/TiO_2 as-formed materials had the appearance of black, grey or brown-coloured powders due to the presence of carbon impurities. All samples were further annealed under air at 450 °C during 6 h in a tubular furnace (Carbolite) to remove residual carbon. The annealed particles were labelled TiO_2-X and Cu/TiO_2-X (X = He, Ar) depending on their synthesis environment. Powder images are provided in Figure S1.

2.3. Samples Characterization

The morphology of prepared photocatalysts was evaluated using transmission electron microscopy (TEM, Tecnai G2 F20 from Fei, Hillsboro, OR, USA).

In order to probe the presence of Cu element, energy-dispersive spectroscopy (EDS) analyses were performed in the scanning transmission electron microscope high-angle annular dark field (STEM-HAADF) imaging mode of a 200 kV Titan-Themis TEM/STEM electron microscope from Fei (Hillsboro, OR, USA) equipped with a Cs probe corrector and a ChemiSTEM Super-X detector (Fei, Hillsboro, OR, USA). These two accessories allow chemical mapping of light and heavy elements with a spatial resolution in the picometer range. The experimental conditions were set so that the total current within the probe used for the STEM-HAADF EDS chemical analysis was about 85 pA.

Samples specific surface areas were determined using N_2 adsorption according to the Brunauer–Emmett–Teller (BET) method with a Micromeritics (Norcross, GA, USA) 3Flex apparatus. Briefly, the BET method is based on the measurement of N_2 gas molecule physisorption onto the solid sample.

Crystalline phases were identified via X-ray diffraction (XRD) measurements using a Bruker D2 Phaser diffractometer (Bruker AXS, Karlsruhe, Germany) with monochromatised Cu Kα radiation (λ = 1.5418 Å). Anatase (JCPDS No. 21-1272) and rutile (JCPDS No. 21-1276) percentages were calculated from the Spurr and Myers equation [17].

XPS measurements were performed on a K-Alpha spectrometer from ThermoFisher, Waltham, MA, USA equipped with a monochromated X-ray source (Al Kα, 1486.7 eV) with a spot size of 400 µm. The hemispherical analyser was operated in CAE (constant analyser energy) mode, with a pass energy of 200 eV and a step of 1 eV for the acquisition of survey spectra and a pass energy of 50 eV and 10 eV and a step of 0.1 eV for the acquisition of narrow scans. The spectra were recorded and treated by means of Avantage software (version 5.967). The binding energy scale was calibrated against the Ti 2p binding energy set at 258.5 eV.

Copper content was measured using inductively coupled plasma optical emission spectroscopy (ICP-OES) with a Jobin Yvon Activa instrument (Horiba, Edison, NJ, USA).

Carbon content was determined by using a Emia-320V Carbon/Sulphur analyser (Horiba, Edison, NJ, USA).

2.4. Photocatalytic Measurements

Photocatalytic runs were carried out in a 250 mL Pyrex photoreactor equipped with a mechanic agitator (500 rpm) and a gas inlet and outlet for gas sampling and purge. A 18W PL-L lamp (Philips, Amsterdam, The Netherlands), placed below the photoreactor, was chosen as the UVA source with a UV band of 350-410 nm centred at 370 nm (irradiance of 5 $mW.cm^{-2}$).

We introduced 100 mL of a 1.0 vol% PA solution containing 50 mg of photocatalyst into the reactor. A continuous flow of argon (70 $mL.min^{-1}$) was applied through a bubbler for 6 h into the system to fully remove the ambient air. After the purge, the photoreactor was sealed and irradiated with UVA light. Every 65 min, a 2 mL aliquot of photoproduced gases in the headspace was carried by vacuum pumping into a Clarus 500 GC FID-PDHID (PerkinElmer, Waltham, MA, USA) for analysis. Products were firstly separated though a RT-Q-Bond (Restek–30 m × 0.53 mm × 20 µm) column before FID with a Polyarc methanization module. For PDHID, a RT-M5A molecular sieve (Restek–30 m × 0.32 mm × 30 µm) was added. The carrier gas was helium N60 grade (Messer, Bad Soden, Germany). For each gaseous analysis, the oven temperature was set at 50 °C rising at 20 °C/min to reach a maximum temperature of 150 °C maintained for an additional 55 min. Tests were repeated twice to ensure reproducibility.

3. Results and Discussion

3.1. Physico-Chemical Properties

3.1.1. Synthesis

It was possible to observe the flame during synthesis experiments through a window. The flame seen in presence of helium was much less bright than under argon, which is an indication of a lower flame temperature under He atmosphere. The temperature appears to

be a major parameter due to the change of atmosphere. The specific heat capacity of helium is 10 times higher than argon, explaining why such a lower temperature was reached in helium atmosphere after laser absorption as well as the fast temperature decrease. As a consequence, the lower temperature observed under He atmosphere explains a lower grain size as well as a lower rutile content in nanoparticles synthesised under He compared to nanoparticles generated under Ar (Table 1 and Figure 1). Similar observations were reported by Pignon et al. [16], who explained these results as a cooling effect of He as well as less efficient confinement of the reactants. Indeed, He is a light gas and is therefore less efficient to confine the reaction. This is also apparent from the lower production rate (i.e., collected powder, Table 1) in He compared to Ar.

Table 1. Characteristics of TiO_2 and Cu_xO_y/TiO_2 elaborated under He and Ar atmospheres. (Unless specified, characterisation results concern annealed powders).

Samples	Production Rate (g/h)	C Content before Annealing (wt%)	Mass Loss after Annealing (%)	BET Surface Area ($m^2.g^{-1}$) (Diameter [a] (nm))	TEM Diameter [b] (nm)	Crystallinity (Phase Fraction)		Cu Content (wt%)
						Anatase	Rutile	
TiO_2-He	5.1	34.5	41	111 (13.6)	15 ± 4	87%	13%	-
TiO_2-Ar	10.3	44.7	49	81 (18.6)	16 ± 6	76%	24%	-
Cu/TiO_2-He	4.5	17.9	22	138 (10.8)	12 ± 3	89%	11%	1.76 ± 0.04
Cu/TiO_2-Ar	9.5	53.9	58	40 (35.7)	31 ± 11	53%	47%	1.91 ± 0.04

[a]: Calculated from 6000/specific surface area (Brunauer–Emmett–Teller, BET) [$m^2.g^{-1}$] × density [g/cm^3]) formula. Density takes into account anatase and rutile proportions determined using XRD as well as Cu content measured via ICP-OES. [b]: Diameter estimated from the measure of 100 particles using ImageJ 1.53t software.

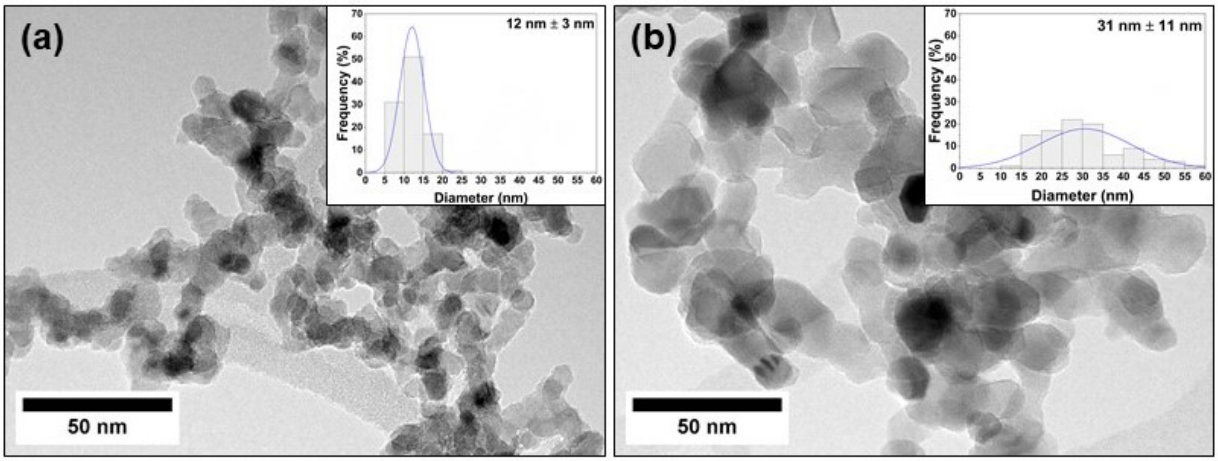


Figure 1. TEM images of annealed Cu/TiO_2-He NPs (**a**) and Cu/TiO_2-Ar NPs (**b**); insets refer to associated size distribution histogram fitted with the normal function.

Table 1 summarises the characteristics of the obtained Cu_xO_y/TiO_2 samples and their TiO_2 references synthesised in similar conditions. In agreement with the more efficient decomposition of precursors, the production rate is higher under Ar atmosphere and carbon content increases in the as-formed TiO_2-Ar and Cu/TiO_2-Ar samples compared to samples obtained under He environment.

After annealing, TiO_2 samples turned white, indicating the efficient removal of carbon species, whereas Cu_xO_y/TiO_2 powders appeared pale green-coloured, suggesting the presence of copper. The associated mass losses are in agreement with the carbon content of the as-formed powders. This result was confirmed with elementary analyses revealing only traces of residual carbon $\leq$0.3 wt% in all the samples.

3.1.2. Morphology and Structure

The morphology of the annealed samples was first investigated by TEM analysis (Figures 1 and S2). From the TEM images, all particles appear to present mostly a spherical shape arranged in chains typical of gas phase synthesis. The average diameters estimated from both BET and TEM measurements are reported in Table 1 and correspond well to each other.

The grain size is larger for nanoparticles synthetised under Ar rather than He environment. Particularly, the diameter of Cu/TiO_2-Ar nanoparticles deduced from the TEM analyses seems to be 1.9 times larger than its bare TiO_2-Ar reference. It seems that the addition of copper element promotes the formation of larger particles. This observation together with the highest rutile content observed in this sample confirms a higher synthesis temperature for Cu/TiO_2-Ar. XRD analyses were performed on all the samples before and after annealing (Figure S3). The samples consist of a mixture of a major anatase phase with a minor rutile phase, except for Cu/TiO_2-Ar (Table 1). Finally, XRD patterns do not reveal peaks associated with copper species, probably due to small crystallite sizes and low Cu content.

UV-visible DRS optical analyses (Figure S4) revealed a band gap between 3.0 and 3.2 eV, in good agreement with anatase (3.2 eV) and rutile (3.0 eV) corresponding ratios in the annealed nanoparticles.

3.1.3. Chemical Analyses

The presence of copper was first confirmed by ICP-OES analysis (Table 1). Cu loadings are consistent regarding the 2.0 wt% Cu content in the liquid precursors. Regarding the copper content, it is slightly higher, with 1.91 $\pm$ 0.04 wt% (Cu/TiO_2-Ar) vs. 1.76 $\pm$ 0.04 wt% (Cu/TiO_2-He) when the argon atmosphere was used. The reaction temperature appears higher when working under argon atmosphere compared to helium atmosphere. This higher temperature induces a better decomposition of copper precursor in argon atmosphere and therefore a slightly higher Cu content in the powder.

High-angle annular dark-field imaging (STEM-HAADF) coupled with EDS chemical analysis was employed in order to evidence the presence as well as the repartition of Ti and Cu elements within the analysed samples. From the STEM-HAADF images illustrated in Figures 2 and S5, the presence of bright spots was detected on the surface of Cu/TiO_2-Ar (Figure 2a,c). The corresponding STEM-HAADF EDS map recorded by considering the Cu Kα edge illustrated in Figure 2b suggests that these bright spots within the Cu/TiO_2-Ar powders are Cu-based nanoparticles localised within the whole TiO_2 support. From these images, we deduce that the size of these NPs is of 1.8 nm $\pm$ 0.3 nm (Figure S6). Moreover, STEM-HAADF EDS line scan analyses performed across the yellow line Cu/TiO_2-Ar (Figure 2c,d) confirm the presence of Cu species into four distinct NPs. Moreover, these Cu NPs appear localised on the surface of TiO_2. On the contrary, STEM-HAADF analyses performed on Cu/TiO_2-He sample (Figure 2e,f) do not show any defined bright spot. The inset on the corresponding EDS-Cu elemental map associated with the Cu/TiO_2-He image (Figure 2f) highlights a very poor contrast between Cu element (in black) and the background (in white). From this inset, it can be seen Cu well-dispersed species across TiO_2 particles. The STEM-HAADF EDS line scan analysis performed along the yellow arrow (Figure 2g,h) confirms that Cu element is homogeneously dispersed within TiO_2, most likely due to the lower specific surface area of TiO_2 nanoparticles when synthetised under He. From this type of analysis, we can sustain that there are significant differences in terms of Cu dispersion and size within the TiO_2 support depending on the material synthesis conditions, i.e., the atmosphere in the present case.

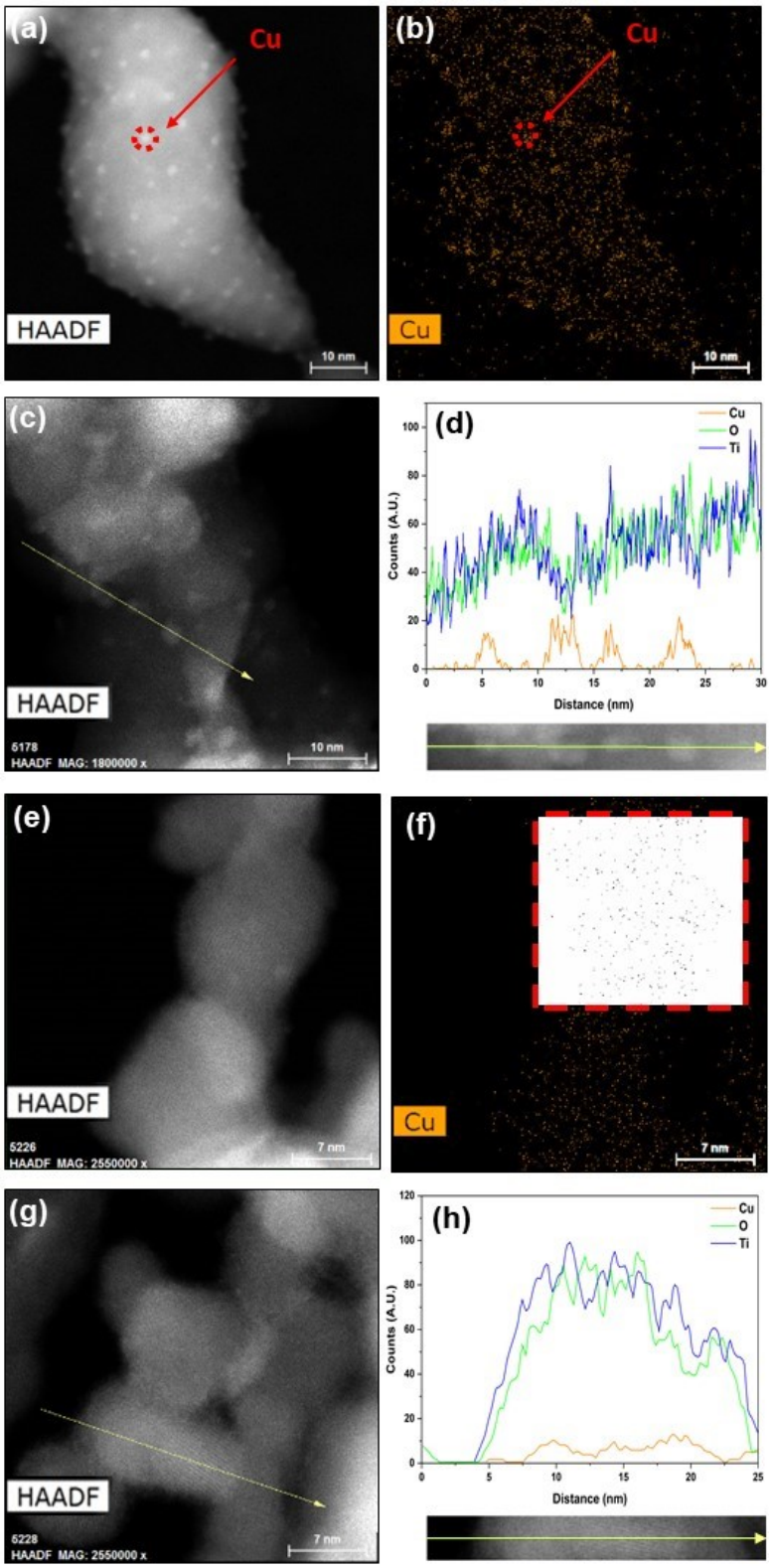


Figure 2. STEM-HAADF images and corresponding Cu elemental maps of Cu/TiO_2-Ar (**a**,**b**) and Cu/TiO_2-He (**e**,**f**) samples; STEM-HAADF images and associated EDS line scan analysis recorded along the yellow arrow performed on Cu/TiO_2-Ar (**c**,**d**) and Cu/TiO_2-He (**g**,**h**). Inset in (**f**) highlights the visualisation of Cu element (black spots on white background) by means of a treatment operated on ImageJ software.

XPS analyses were conducted to investigate the surface chemical state of elements in both TiO_2 and Cu_xO_y/TiO_2 synthetised under different atmospheres. Figure S7 depicts the XPS full spectra of pure TiO_2 and Cu/TiO_2, which shows the presence of, Ti, O, and C for all samples. In addition, Cu element appeared in both Cu/TiO_2-He and Cu/TiO_2-Ar powders. The Ti 2p core-level spectrum of TiO_2 (Table 2 and Figure S8a,b) consists of two peaks centred at 464.2 and 458.5 eV, corresponding to Ti $2p_{1/2}$ and Ti $2p_{3/2}$ of Ti^{4+}, respectively [18]. A broadening of the Ti 2p doublet is observed for Cu_xO_y/TiO_2 samples in comparison to TiO_2 references (Table 2). Indeed, Ti $2p^{3/2}$ FWHM corresponds to 1.1 eV for both TiO_2-He and TiO_2-Ar and increases to 1.3 eV and 1.5 eV for the Cu/TiO_2-He and Cu/TiO_2-Ar samples, respectively. This suggests an interaction between copper species and TiO_2 through the incorporation of Cu ions in TiO_2 lattice [19,20].

Table 2. XPS analysis of TiO_2 and Cu_xO_y/TiO_2 elaborated under He and Ar atmospheres.

Samples	Ti $2p_{3/2}$ (eV) [18]		Cu $2p_{3/2}$ (eV) [18,21]		Cu^{2+} (at%)	Cu/Ti
	BE	FWHM	Cu^0 + Cu^+	Cu^{2+}		
TiO_2-He	458.5	1.1	-	-	-	-
Cu/TiO_2-He	458.5	1.3	932.5	933.3; 934.9	36.7	0.06
TiO_2-Ar	458.5	1.1	-	-	-	-
Cu/TiO_2-Ar	458.5	1.5	932.4	933.1; 934.7	49.3	0.14

The Cu $2p_{3/2}$ core-level spectrum (Figure 3) reveals several co-existing Cu chemical states in Cu/TiO_2-He and Cu/TiO_2-Ar [18,21]. The peaks at 934.8 eV and 933.2 eV are assigned to the Cu^{2+} $2p_{3/2}$ signal of $Cu(OH)_2$ and CuO, respectively. Shake-up satellite peaks confirm the presence of Cu^{2+}. Additionally, the component at about 932.5 eV refers to both the Cu^0 and Cu^+ $2p_{3/2}$ signal, as the two oxidation states cannot be distinguished, having very close binding energies. By comparing Cu^{2+} proportions, it seems that copper species are more reduced in the Cu/TiO_2-He sample. XPS quantification reveals copper content of 4.1 wt% and 9.2 wt% for Cu/TiO_2-He and Cu/TiO_2-Ar, respectively. This is 2.3 and 4.9 times higher than bulk values provided by ICP-OES analyses, confirming a significant segregation of copper species on the surface of TiO_2, clearly pronounced in the case of the Cu/TiO_2-Ar sample. In addition, the Cu/Ti ratio is lower for Cu/TiO_2-He, which could be attributed to a higher dispersion on the support [22,23], confirming our previous results.

Finally, the TiO_2 and Cu_xO_y/TiO_2 nanoparticles obtained by laser pyrolysis exhibit distinct morphologies: the Cu/TiO_2-He sample consists of nanoparticles of 10 nm range, including very well dispersed Cu species on TiO_2, whereas the Cu/TiO_2-Ar particles are about 30 nm, with defined copper-based nanoparticles of about 2 nm size on the TiO_2 support.

3.2. Photocatalytic PA Degradation in Anaerobic Media

The main gases photoproduced from PA degradation under anaerobic conditions are presented in Figure 4 and a typical chromatogram is shown in Figure S9. The identified gases are CO_2, ethylene C_2H_4, ethane C_2H_6 and H_2. Butane C_4H_{10} (Figure S10) was detected as a minor product. The principal mechanisms for saturated carboxylic acid degradation in oxygen-free media with pure TiO_2 or decorated with noble metals have already been reported [11,13]. The first step consists of the decarboxylation of carboxylic acid through reaction with photo-generated trapped holes (Equation (1)):

$$CH_3CH_2COOH + h^+ \rightarrow CH_3CH_2\bullet + CO_2 + H^+, \quad (1)$$

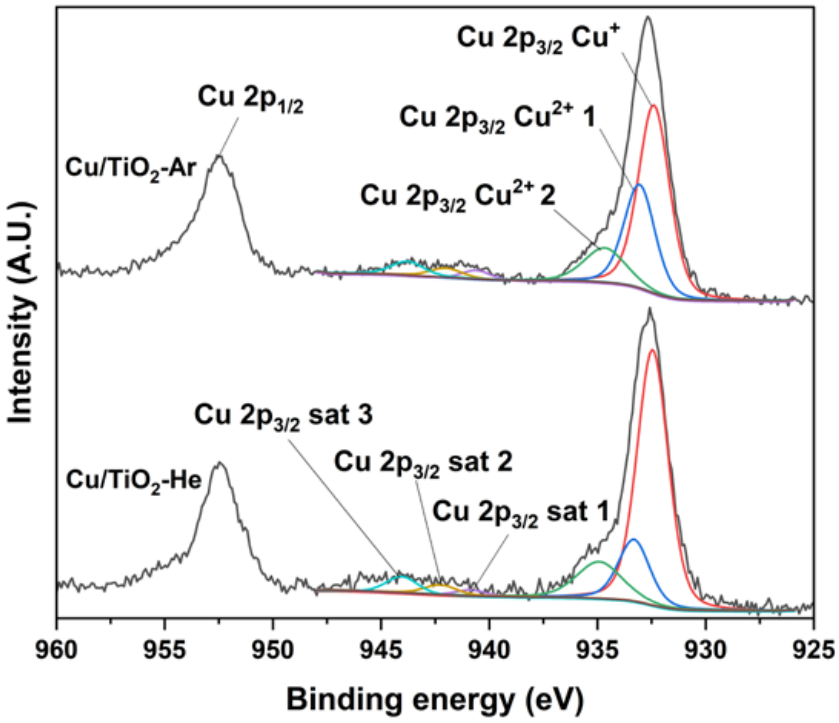


Figure 3. Cu 2p core-level spectra comparison of Cu/TiO_2-He and Cu/TiO_2-Ar samples.

The $CH_3CH_2\bullet$ radical can react with a H• ($H^+ + e^-$) to further form C_2H_6 in majority. The coupling of two $CH_3CH_2\bullet$ is responsible for C_4H_{10} formation, and two H• can form H_2. According to Scandura et al. [10], traces of ethylene are formed by the reaction of $CH_3CH_2\bullet$ with h^+. Hence, from Equation (1), selectivities are defined in terms of hydrocarbon (C_2H_4, C_2H_6) to CO_2 ratio.

Several differences can be seen from Figure 4. With pristine TiO_2 (black and blue curves, Figure 4), the main products are CO_2 and C_2H_6 (C_2H_6/CO_2 = 73% and 68% for TiO_2-He and TiO_2-Ar, respectively). The slightly different photoactivities of TiO_2-He and TiO_2-Ar observed for CO_2 and C_2H_6 productions could be correlated with different anatase to rutile ratios (i.e., presence of junction) as well as different BET surface areas. It is known that the presence of a junction enhances activity through more efficient electron transfer; see, for example [24,25]. However, in the present case, it is difficult to conclude if the slightly better efficiency of TiO_2-He is related to its largest surface area (111 vs. 81 $m^2.g^{-1}$) or to the change in anatase to rutile ratio (87 vs. 76% of anatase). H_2 and C_2H_4 (C_2H_4/CO_2 = 1%) are identified in trace amounts, in agreement with the literature in the absence of co-catalysts for H_2 [26–28] or with the use of noble metals (Pt, Au) for C_2H_4 [10–12].

Surface modifications of TiO_2 photocatalysts with copper/copper oxides leads to drastic changes in terms of levels of photo-generated products. Notably, Cu/TiO_2-He appears as the most efficient photocatalyst for CO_2, C_2H_6, and C_4H_{10} production (Figure S9), with C_2H_6 as the major hydrocarbon (green curve, Figure 4). C_2H_4 formation is enhanced (C_2H_4/CO_2 = 11%) until 200 min of reaction, then it slows down. On the contrary, H_2 production is increased from this same irradiation time (200 min). These phenomena could be attributed to the efficiency of the Cu_xO_y-TiO_2 heterojunction that decreases electron–hole recombination [29,30], but above all thanks to the reduction of copper oxides into metallic copper [31–33]. Indeed, well-dispersed copper species on the TiO_2 surface in the Cu/TiO_2-He sample could be reduced after about 200 min of UV irradiation. Therefore, Cu^0, acting as an e^- scavenger, highly enhances H_2 formation. The $CH_3CH_2\bullet$ radical preferentially reacting with a H• formed on the Cu^0 site could explain how reduced copper species inhibit the formation of C_2H_4 while enhancing C_2H_6 production.

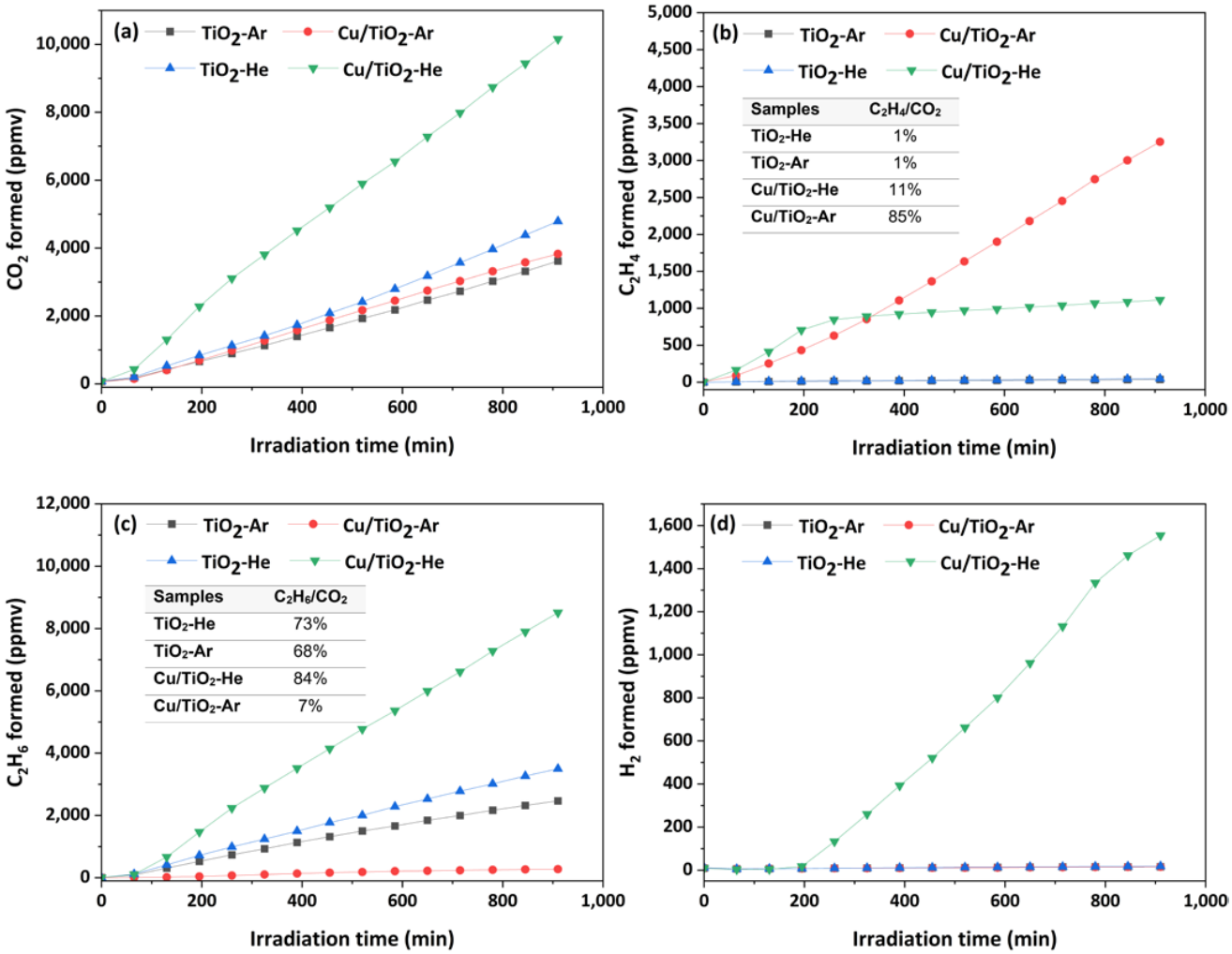


Figure 4. Major products formed from the photo-decarboxylation of PA (1 vol%) under UVA light: CO_2 (**a**), C_2H_4 (**b**), C_2H_6 (**c**), H_2 (**d**). Ratios are calculated at 910 min of irradiation (see also Figure S11).

Remarkably, Cu/TiO_2-Ar (red curve, Figure 4) is the most efficient material for C_2H_4 production: it is the major hydrocarbon product with a C_2H_4/CO_2 ratio in the range = 85–88%. Its formation evolves linearly at 260 ppmv/h, 130 times greater than the production rate reached from pure titania. This efficient production is obtained at the expense of C_2H_6 (C_2H_6/CO_2 = 4–7%) and H_2 formation. This contrasting behaviour compared to Cu/TiO_2-He may be related to less-dispersed, larger, and oxidised copper nanoparticles on TiO_2 support, as seen in STEM-HAADF/EDS and XPS characterizations. The larger size allows Cu_xO_y NPs to resist complete photo-reduction, as reported by Imizcoz et al. [31]. In addition, according to Yu et al. [29], a larger Cu_xO_y size limits the direct transfer of electrons from Cu_xO_y to H^+ due to a decrease in the conduction band. Consequently, H_2 and C_2H_6 formations are not favoured. These particular conditions seem to enhance C_2H_4 production, as observed in the present study.

4. Conclusions

This study reports for the first time the significant production of C_2H_4 molecules from the photocatalytic degradation of propionic acid. TiO_2 nanoparticles modified with Cu_xO_y used as photocatalysts were prepared using the laser pyrolysis synthesis method. The atmosphere of synthesis (argon or helium) strongly modifies Cu_xO_y/TiO_2 morphologies as well as their photocatalytic properties. Cu_xO_y/TiO_2 obtained under helium consist

of small TiO_2 nanoparticles with highly dispersed copper species that could be reduced into Cu^0 under UV irradiation. These reduced species promote the formation of H_2 and C_2H_6 at the expense of C_2H_4. On the contrary, larger Cu_xO_y/TiO_2 NPs were obtained under argon atmosphere with defined Cu_xO_y nanoparticles (1–2 nm diameter) on the surface of TiO_2. It seems that such less-dispersed Cu_xO_y nanoparticles inhibit H_2 and C_2H_6 formation. The major hydrocarbon was C_2H_4, with an outstanding selectivity higher than 85%, outperforming by 130 times the ethylene production from pristine TiO_2. Although the ethylene formation mechanism should be further examined, this study paves the way to a new energy-saving method to produce C_2H_4 from organic acid without noble-metal-based photocatalysts.

Supplementary Materials: The following supporting information can be downloaded at: https://www.mdpi.com/article/10.3390/nano13050792/s1, Figure S1: Images of TiO_2 and Cu/TiO_2 samples before (a) and (b) after annealing; Figure S2: TEM images and associated histograms of size distribution of TiO_2 powders. Diameter measurements were performed on 100 particles with ImageJ software; Figure S3: XRD patterns of Cu/TiO_2 samples before and after annealing (a); TiO_2 and associated Cu/TiO_2 samples after annealing (b); XRD patterns of TiO_2 and Cu/TiO_2 as formed (c); Figure S4: Optical gap determination from UV-vis diffuse reflectance spectra using modified Kubelka–Munk function considering indirect gap of TiO_2; Figure S5: HAADF-STEM and Ti, O, Cu elemental maps performed on Cu/TiO_2-Ar (a) and Cu/TiO_2-He (b); Figure S6: Histograms of size distribution of Cu nanoparticles in Cu/TiO_2-Ar. Diameter measures were realised on 40 particles with ImageJ software; Figure S7: XPS survey spectra of synthetised TiO_2 and Cu/TiO_2; Figure S8: Ti 2p (a,b), O 1s (c,d) and C 1s (e,f) core-level spectra of synthetised TiO_2 and Cu/TiO_2; Figure S9: FID (Flame Ionization Detector) gas chromatogram of after 910 minutes of irradiation from PA (1 vol%) photo-decarboxylation with Cu/TiO_2-Ar. Gas identifications were made with calibration cylinders of CO_2 alone (1000 ppm in nitrogen), C_2H_6 alone (500 ppm in nitrogen) and a mixture of C_2H_6 and C_2H_4 (10 ppm in nitrogen). Retention times (min) are in green. Figure S10. C_4H_{10} formation from PA (1 vol%) photo-decarboxylation under UVA light. C_4H_{10}/CO_2 ratios are calculated at 910 min of irradiation, Figure S11. Carbon equivalent of each detected product by GC after 910 min of irradiation of PA (1 vol%). Calculations are made considering 1 CO_2 molecule for 1 C2 product (C_2H_4, C_2H_6, acetal-dehyde) and 2 CO_2 molecules for C4 product (C_4H_{10}). Reference [34] is cited in supplementary materials.

Author Contributions: J.K., P.L. and N.H.-B. performed synthesis of samples. J.K. and F.D. performed photocatalytic tests. D.D. obtained and analysed XPS data. I.F. performed STEM analysis. N.H.-B. and C.G. directed this study. All authors were involved in writing the manuscript. All authors have read and agreed to the published version of the manuscript.

Funding: This research received no external funding.

Institutional Review Board Statement: Not applicable.

Informed Consent Statement: Not applicable.

Data Availability Statement: The data that support the findings of this study are available from the authors on reasonable request.

Acknowledgments: STEM-HAADF/EDS chemical analyses were performed in the frame of the French Government Program of Investment for the Future (Programme d'Investissement d'Avenir–TEMPOS Equipex–ANR-10-EQPX-50, pole NanoTEM). The authors would also like to acknowledge the Centre Interdisciplinaire de Microscopie électronique de l'X (CIMEX).

Conflicts of Interest: The authors declare no conflict of interest.

References

1. Zhang, M.; Yu, Y. Dehydration of Ethanol to Ethylene. *Ind. Eng. Chem. Res.* **2013**, *52*, 9505–9514. [CrossRef]
2. Zimmermann, H.; Walzl, R. Ethylene. In *Ullmann's Encyclopedia of Industrial Chemistry*; Weinheim Wiley-VCH: Weinheim, Germany, 2000.
3. Bai, P.T.; Rajmohan, K.S.; Prasad, P.S.S.; Srinath, S. *Oxidative Dehydrogenation of Ethane to Ethylene Over Metal Oxide Catalysts Using Carbon Dioxide*; Springer: Singapore, 2019; ISBN 9789811332968.

4. Haribal, V.P.; Chen, Y.; Neal, L.; Li, F. Intensification of Ethylene Production from Naphtha via a Redox Oxy-Cracking Scheme: Process Simulations and Analysis. *Engineering* **2018**, *4*, 714–721. [CrossRef]
5. Ren, T.; Patel, M.; Blok, K. Olefins from Conventional and Heavy Feedstocks: Energy Use in Steam Cracking and Alternative Processes. *Energy* **2006**, *31*, 425–451. [CrossRef]
6. Palmisano, G.; Augugliaro, V.; Pagliaro, M.; Palmisano, L. Photocatalysis: A Promising Route for 21st Century Organic Chemistry. *Chem. Commun.* **2007**, *33*, 3425–3437. [CrossRef] [PubMed]
7. Zhang, H.; Li, M.M.J. Crafting an Active Center with a Local Charge Density Gradient to Facilitate Photocatalytic Ethylene Production from CO_2. *Curr. Opin. Green Sustain. Chem.* **2022**, *36*, 100646. [CrossRef]
8. Guillard, C. Photocatalytic Degradation of Butanoic Acid: Influence of Its Ionisation State on the Degradation Pathway: Comparison with O3/UV Process. *J. Photochem. Photobiol. A Chem.* **2000**, *135*, 65–75. [CrossRef]
9. Scandura, G.; Rodríguez, J.; Palmisano, G. Hydrogen and Propane Production from Butyric Acid Photoreforming Over Pt-TiO_2. *Front. Chem.* **2019**, *7*, 563. [CrossRef]
10. Scandura, G.; Sajjad, M.; Singh, N.; Palmisano, G.; Rodríguez, J. On the Selectivity of Butyric Acid Photoreforming over Au/TiO_2 and Pt/TiO_2 by UV and Visible Radiation: A Combined Experimental and Theoretical Study. *Appl. Catal. A Gen.* **2021**, *624*, 118321. [CrossRef]
11. Kraeutler, B.; Bard, A.J. Heteogeneous Photocatalytic Decomposition of Saturated Carboxylic Acids on TiO_2 Powder. Decarboxylative Route to Alkanes. *J. Am. Chem. Soc.* **1978**, *100*, 5985–5992. [CrossRef]
12. Betts, L.M.; Dappozze, F.; Guillard, C. Understanding the Photocatalytic Degradation by P25 TiO_2 of Acetic Acid and Propionic Acid in the Pursuit of Alkane Production. *Appl. Catal. A Gen.* **2018**, *554*, 35–43. [CrossRef]
13. Sakata, T.; Kawai, T.; Hashimoto, K. Heterogeneous Photocatalytic Reactions of Organic Acids and Water. New Reaction Paths besides the Photo-Kolbe Reaction. *J. Phys. Chem.* **1984**, *88*, 2344–2350. [CrossRef]
14. Zhang, N.; Liu, S.; Fu, X.; Xu, Y.J. Synthesis of M@TiO_2 (M = Au, Pd, Pt) Core-Shell Nanocomposites with Tunable Photoreactivity. *J. Phys. Chem. C* **2011**, *115*, 9136–9145. [CrossRef]
15. Chen, Y.; Zhang, X.; Chen, Y. Propionic Acid-Rich Fermentation (PARF) Production from Organic Wastes: A Review. *Bioresour. Technol.* **2021**, *339*, 125569. [CrossRef] [PubMed]
16. Pignon, B.; Maskrot, H.; Ferreol, V.G.; Leconte, Y.; Coste, S.; Gervais, M.; Pouget, T.; Reynaud, C.; Tranchant, J.F.; Herlin-Boime, N. Versatility of Laser Pyrolysis Applied to the Synthesis of TiO_2 Nanoparticles—Application to UV Attenuation. *Eur. J. Inorg. Chem.* **2008**, *2008*, 883–889. [CrossRef]
17. Spurr, R.A.; Myers, H. Quantitative Analysis of Anatase-Rutile Mixtures with an X-ray Diffractometer. *Anal. Chem.* **1957**, *29*, 760–762. [CrossRef]
18. Biesinger, M.C.; Lau, L.W.M.; Gerson, A.R.; Smart, R.S.C. Resolving Surface Chemical States in XPS Analysis of First Row Transition Metals, Oxides and Hydroxides: Sc, Ti, V, Cu and Zn. *Appl. Surf. Sci.* **2010**, *257*, 887–898. [CrossRef]
19. Valero, J.M.; Obregón, S.; Colón, G. Active Site Considerations on the Photocatalytic H_2 Evolution Performance of Cu-Doped TiO_2 Obtained by Different Doping Methods. *ACS Catal.* **2014**, *4*, 3320–3329. [CrossRef]
20. Pham, T.D.; Lee, B.K. Disinfection of Staphylococcus Aureus in Indoor Aerosols Using Cu-TiO_2 Deposited on Glass Fiber under Visible Light Irradiation. *J. Photochem. Photobiol. A Chem.* **2015**, *307–308*, 16–22. [CrossRef]
21. Liu, Z.; Zhou, C. Improved Photocatalytic Activity of Nano CuO-Incorporated TiO_2 Granules Prepared by Spray Drying. *Prog. Nat. Sci. Mater. Int.* **2015**, *25*, 334–341. [CrossRef]
22. Obregón, S.; Muñoz-Batista, M.J.; Fernández-García, M.; Kubacka, A.; Colón, G. Cu-TiO_2 Systems for the Photocatalytic H_2 Production: Influence of Structural and Surface Support Features. *Appl. Catal. B Environ.* **2015**, *179*, 468–478. [CrossRef]
23. Ilie, M.; Cojocaru, B.; Parvulescu, V.I.; Garcia, H. Improving TiO_2 Activity in Photo-Production of Hydrogen from Sugar Industry Wastewaters. *Int. J. Hydrogen Energy* **2011**, *36*, 15509–15518. [CrossRef]
24. Wang, F.; Pei, K.; Li, Y.; Li, H.; Zhai, T. 2D Homojunctions for Electronics and Optoelectronics. *Adv. Mater.* **2021**, *33*, 2005303. [CrossRef] [PubMed]
25. Assayehegn, E.; Solaiappan, A.; Chebude, Y.; Alemayehu, E. Fabrication of Tunable Anatase/Rutile Heterojunction N/TiO_2 Nanophotocatalyst for Enhanced Visible Light Degradation Activity. *Appl. Surf. Sci.* **2020**, *515*, 145966. [CrossRef]
26. Al-Azri, Z.H.N.; Chen, W.T.; Chan, A.; Jovic, V.; Ina, T.; Idriss, H.; Waterhouse, G.I.N. The Roles of Metal Co-Catalysts and Reaction Media in Photocatalytic Hydrogen Production: Performance Evaluation of M/TiO_2 Photocatalysts (M = Pd, Pt, Au) in Different Alcohol-Water Mixtures. *J. Catal.* **2015**, *329*, 355–367. [CrossRef]
27. Tran, P.D.; Xi, L.; Batabyal, S.K.; Wong, L.H.; Barber, J.; Chye Loo, J.S. Enhancing the Photocatalytic Efficiency of TiO_2 Nanopowders for H_2 Production by Using Non-Noble Transition Metal Co-Catalysts. *Phys. Chem. Chem. Phys.* **2012**, *14*, 11596–11599. [CrossRef] [PubMed]
28. Lan, L.; Daly, H.; Jiao, Y.; Yan, Y.; Hardacre, C.; Fan, X. Comparative Study of the Effect of TiO_2 Support Composition and Pt Loading on the Performance of Pt/TiO_2 Photocatalysts for Catalytic Photoreforming of Cellulose. *Int. J. Hydrogen Energy* **2021**, *46*, 31054–31066. [CrossRef]
29. Yu, J.; Hai, Y.; Jaroniec, M. Photocatalytic Hydrogen Production over CuO-Modified Titania. *J. Colloid Interface Sci.* **2011**, *357*, 223–228. [CrossRef] [PubMed]
30. Li, L.; Xu, L.; Shi, W.; Guan, J. Facile Preparation and Size-Dependent Photocatalytic Activity of Cu_2O Nanocrystals Modified Titania for Hydrogen Evolution. *Int. J. Hydrogen Energy* **2013**, *38*, 816–822. [CrossRef]

31. Imizcoz, M.; Puga, A.V. Optimising Hydrogen Production: Via Solar Acetic Acid Photoreforming on Cu/TiO_2. *Catal. Sci. Technol.* **2019**, *9*, 1098–1102. [CrossRef]
32. Christoforidis, K.C.; Fornasiero, P. Photocatalysis for Hydrogen Production and CO_2 Reduction: The Case of Copper-Catalysts. *ChemCatChem* **2019**, *11*, 368–382. [CrossRef]
33. Jung, M.; Scott, J.; Ng, Y.H.; Jiang, Y.; Amal, R. Impact of Cu Oxidation State on Photocatalytic H_2 Production by Cu/TiO_2. In Proceedings of the 2014 International Conference on Nanoscience and Nanotechnology, ICONN 2014, Adelaide, Australia, 2–6 February 2014; pp. 4–6. [CrossRef]
34. Simmons, E.L. Diffuse reflectance spectroscopy: A comparison of the theories. *Appl. Opt.* **1975**, *14*, 1380–1386. [CrossRef] [PubMed]

Disclaimer/Publisher's Note: The statements, opinions and data contained in all publications are solely those of the individual author(s) and contributor(s) and not of MDPI and/or the editor(s). MDPI and/or the editor(s) disclaim responsibility for any injury to people or property resulting from any ideas, methods, instructions or products referred to in the content.